



Particle image velocimetry measurements of Mach 3 turbulent boundary layers at low Reynolds numbers

J. M. Brooks¹ · A. K. Gupta¹ · M. S. Smith² · E. C. Marineau²

Received: 24 November 2017 / Revised: 30 March 2018 / Accepted: 5 April 2018 / Published online: 25 April 2018
© Springer-Verlag GmbH Germany, part of Springer Nature 2018

Abstract

Particle image velocimetry (PIV) measurements of Mach 3 turbulent boundary layers (TBL) have been performed under low Reynolds number conditions, $Re_\tau = 200\text{--}1000$, typical of direct numerical simulations (DNS). Three reservoir pressures and three measurement locations create an overlap in parameter space at one research facility. This allows us to assess the effects of Reynolds number, particle response and boundary layer thickness separate from facility specific experimental apparatus or methods. The Morkovin-scaled streamwise fluctuating velocity profiles agree well with published experimental and numerical data and show a small standard deviation among the nine test conditions. The wall-normal fluctuating velocity profiles show larger variations which appears to be due to particle lag. Prior to the current study, no detailed experimental study characterizing the effect of Stokes number on attenuating wall-normal fluctuating velocities has been performed. A linear variation is found between the Stokes number (St) and the relative error in wall-normal fluctuating velocity magnitude (compared to hot wire anemometry data from Klebanoff, Characteristics of Turbulence in a Boundary Layer with Zero Pressure Gradient. Tech. Rep. NACA-TR-1247, National Advisory Committee for Aeronautics, Springfield, Virginia, 1955). The relative error ranges from about 10% for $St = 0.26$ to over 50% for $St = 1.06$. Particle lag and spatial resolution are shown to act as low-pass filters on the fluctuating velocity power spectral densities which limit the measurable energy content. The wall-normal component appears more susceptible to these effects due to the flatter spectrum profile which indicates that there is additional energy at higher wave numbers not measured by PIV. The upstream inclination and spatial correlation extent of coherent turbulent structures agree well with published data including those using krypton tagging velocimetry (KTV) performed at the same facility.

1 Introduction

This work is part of the PIV development for use in Arnold Engineering Development Complex (AEDC) Tunnel 9. The objective is to measure a turbulent boundary layer and shock turbulent boundary layer interaction of a hollow cylinder flare test article at Mach 10 with a Reynolds number of $16 \times 10^6/m$, see Brooks et al. (2017). The development process began with sub-scale experiments conducted in the Mach 3 Aero Calibration Laboratory wind tunnel facility (M3CT) also located at AEDC White Oak. Here, the technique was demonstrated and several parameters were

investigated prior to transition into Tunnel 9. The flow field of study is a canonical supersonic turbulent boundary layer. Good agreement between the PIV measurements, theory and literature will provide confidence in the ability of the particles to follow turbulent eddies in the flow. Using the M3CT design operating conditions, the maximum achievable Stokes numbers are between $\sim 0.26\text{--}0.60$. Orifice plates were used to reduce the Reynolds number in the M3CT. This allowed us to generate Stokes numbers comparable to that achieved in Tunnel 9. In addition, reducing the Reynolds number brings the flow conditions closer to those achieved in direct numerical simulation (DNS), with the exception of a few high-Reynolds number studies such as those completed by Pirozzoli (2011) and Pirozzoli and Bernardini (2013). A wide range of reservoir pressures, measurement locations, and camera magnifications create an overlap in the parameter space in one research facility. This allows us to assess the effect of the flow conditions and PIV parameters on the measurements.

✉ J. M. Brooks
jbrook10@umd.edu

¹ University of Maryland, College Park, MD 20742, USA

² AEDC White Oak, 10905 New Hampshire Avenue,
Silver Spring, MD 20903, USA

Flat-plate turbulent boundary layers are well-studied canonical flows Fernholz and Finley (1980); Coles (1956); van Driest (1951); Townsend (1951). The most well-known experimental data are the hot wire anemometry (HWA) measurements conducted by Klebanoff (1955). However, there exist large variations between supersonic turbulent fluctuating velocity profiles reported in the literature which remain largely unresolved. These data not only include particle-based techniques, such as particle image velocimetry (PIV) Ekoto et al. (2007); Pionniau (2009); Lapsa and Dahm (2011) and laser Doppler velocimetry (LDV) Elena and LaCharme (1988), but also HWA Elena and LaCharme (1988); Smits et al. (1983); Kistler (1959) and krypton tagging velocimetry (KTV) Zahradka et al. (2016); Mustafa et al. (2017). Therefore, effects from the particle response are not the sole mechanism for the variations between experiments. Williams et al. (2018) presented a detailed analysis of uncertainties that could contribute to these variations. These authors cite frequency response and spatial resolution as contributing factors to HWA uncertainty and spatial resolution and particle response as contributing factors to PIV uncertainty. However, these effects do not completely explain the variations in data from the literature. For example, there is good agreement between HWA and LDV data from Elena and LaCharme (1988).

Figure 1, partially reproduced from Elena and LaCharme (1988), gives a representation of the extent of the variations. Eléna and LaCharme established limits for these variations from published HWA data, under a range of Mach numbers from 1.7 to 4.7 with outer limits from Smits et al. (1983) and Kistler (1959). Eléna and LaCharme

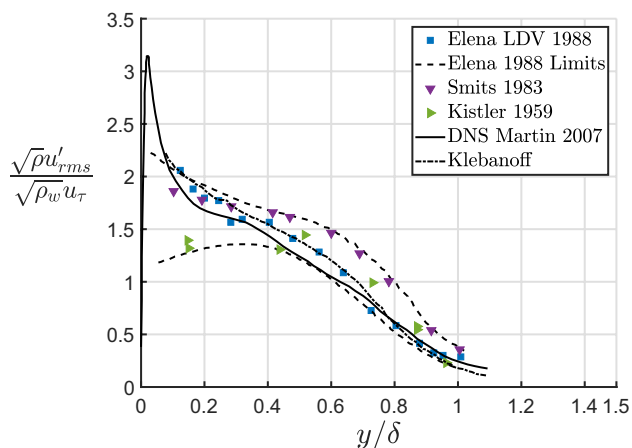


Fig. 1 Morkovin-scaled streamwise fluctuating velocity profile, reproduced from Elena and LaCharme (1988), to show the spread of data in the literature. $M = 2.32$ LDV data and $1.7 < M < 4.7$ HWA data limits from Elena and LaCharme (1988), $M = 2.9$ HWA from Smits et al. (1983), $M = 3.56$ HWA from Kistler (1959), $M = 2.32$ DNS from Martin (2007), incompressible HWA data from Klebanoff (1955)

noted that the reason for the spread remains unexplained. LDV data from Eléna and LaCharme showed very good agreement with incompressible HWA data from Klebanoff. Eléna and LaCharme noted that the better agreement than other LDV published data was due to improvements with LDV seeding.

This paper presents PIV measurements in a Mach 2.7 turbulent boundary layer to characterize the effect of the Reynolds number, Stokes number, and spatial resolution on the measurements. We present the effect of spatial resolution on fluctuating velocity magnitudes by independently varying the camera magnification and the interrogation window size. Mean streamwise velocity profiles are compared to boundary layer theory using inner scaling. Fluctuating streamwise and wall-normal velocity profiles as well as Reynolds shear stress profiles are also presented. Also, the effect of the Stokes number on the wall-normal fluctuating velocity magnitude is assessed. The measurements are compared against DNS for supersonic turbulent boundary layers from Pirozzoli (2011) and Duan et al. (2011) as well as PIV Ekoto et al. (2007); Pionniau (2009); Lapsa and Dahm (2011), LDV Elena and LaCharme (1988), HWA Klebanoff (1955), and krypton tagging velocimetry (KTV) Zahradka et al. (2016). Power spectra densities (PSD) of the streamwise and wall-normal fluctuating velocities are shown to illustrate the effect of particle response and window resolution on the resolved energy content. Contours of streamwise correlation coefficients are presented to determine the angle and scale of the large-scale motion (LSM) turbulent structures.

2 Experimental setup

2.1 Mach 3 Aero Calibration Laboratory wind tunnel

The Mach 3 Aero Calibration Laboratory wind tunnel facility (M3CT) at AEDC White Oak is an indraft supersonic wind tunnel with measured freestream Mach numbers ranging from 2.7 to 2.8. The M3CT is used to develop and demonstrate measurement techniques prior to deployment in Tunnel 9. Under nominal conditions, a large vacuum tank downstream of the 63.5×63.5 mm² test section accelerates ambient room air through a 2-D converging diverging nozzle to provide a test time of approximately 10 s. The test section, schematically shown in Fig. 2, has three measurement locations with modular top/bottom and side inserts. Originally designed for solid aluminum blank and aluminum-framed glass window inserts, the modular design allows additional tunnel components such as clear polycarbonate or acrylic inserts, seeding injector blocks, single Pitot probe and Pitot rake (see Brooks et al. 2014, 2015).

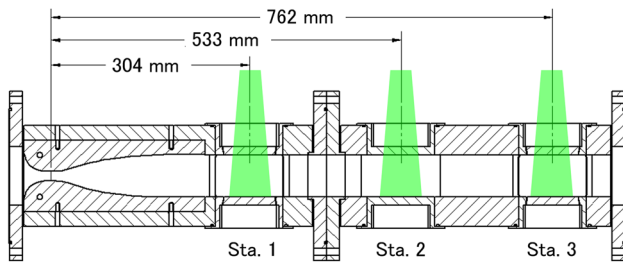


Fig. 2 Schematic of M3CT test section (mid-spanwise cross section) showing distance to the three measurement locations relative to the nozzle throat

Table 1 Orifice plate reservoir conditions

Orifice plate diameter (mm)	p_r (kPa)	T_r (K)
–	101.3	307
25.4	50.1	308
19.1	29.5	306

2.2 Flow conditions

The flow field measured for this study is the zero pressure gradient (ZPG) turbulent boundary layer that develops on the tunnel wall downstream of the nozzle expansion. The recovery temperature is very close to the wall temperature; therefore, the wall is assumed to be adiabatic. The extended length of the test section allows for the growth of a thick turbulent boundary layer, on the order of 10 mm. Although the M3CT operates at relatively low Reynolds number, the Reynolds number was further reduced to more closely compare the particle response time to that estimated for Tunnel 9. The Reynolds number was reduced using orifice plates upstream of the nozzle, as outlined by Zahradka et al. (2016). The orifice plates limit the flow rate, which reduces the reservoir pressure. A series of screens connected by large diameter (152 mm) piping break up the turbulence induced from the jet at the orifice. Two orifice plates were used to

generate three reservoir pressure conditions including use without orifice plate. The reservoir conditions are shown in Table 1.

The flow was determined to transition to turbulence naturally under nominal conditions (without orifice plate) in a previous study by Brooks et al. (2015). The transition location was determined using laminar and turbulent solutions of the Virginia Tech Boundary Layer Applet (Devenport and Schetz 1998; Devenport et al. 1999). The starting location of the turbulent solution was varied to match the boundary layer thickness to the PIV data at the measurement section. This analysis revealed that the flow transitioned in the diverging portion of the nozzle. When using an orifice plate, the reduced Reynolds number pushes the transition point further downstream. In certain cases the flow transitioned at the measurement location. To ensure a fully turbulent boundary layer, trips were installed in the subsonic section of the nozzle. The trips were designed to minimize flow disturbances, while still generating the desired well-developed turbulent flowfield at the first measurement station. For the 25.4-mm orifice, a distributed roughness strip was made from 120 grit sandpaper. The $12.7 \times 60.3 \text{ mm}^2$ strip was attached with double-sided tape. For the 19.1-mm orifice, two 1.65-mm-thick Teflon tape trips measuring $9.5 \times 60.3 \text{ mm}^2$ were installed. Trip sizes were determined experimentally by PIV through the verification of a turbulent boundary layer profile.

The flow conditions for all nine configurations are presented in Table 2. The multiple measurement locations and orifice diameters set up an overlapping parameter space in terms of Reynolds number, boundary layer thickness and PIV particle Stokes number. Mean velocities were ensemble averaged over all image pairs and over a streamwise distance on the order of $1-2\delta$ for a total of about 10,000–50,000 realizations (approximately 620 frames) at each y/δ location over 0.07. The reservoir and freestream conditions, in Tables 1 and 2, respectively, are calculated from the PIV and Pitot-static pressure measurements. The Mach number was obtained using a Pitot probe in the freestream and a

Table 2 M3CT reduced Reynolds number flow conditions

Experiment	Station	Position	Orifice	M_e	u_e	Re_m	δ	θ	Re_θ	Re_τ	St	Π
Ref. Code	No.	(mm)	(mm)		(m/s)	(1/m)	(mm)	(mm)				
1A	143	300	19.1	2.8	621	$2.3e+06$	8.2	0.52	1167	202	1.09	0.54
1B	146	300	25.4	2.8	620	$3.9e+06$	6.6	0.41	1603	273	0.87	0.42
1C	153	300	–	2.8	623	$7.7e+06$	5.8	0.34	2631	446	0.60	0.49
2A	162	530	19.1	2.8	610	$2.4e+06$	12.4	0.82	1963	304	0.67	0.57
2B	161	530	25.4	2.8	607	$4.2e+06$	10.3	0.67	2811	420	0.51	0.50
2C	154	530	–	2.8	605	$8.4e+06$	8.6	0.57	4767	657	0.37	0.54
3A	169	760	19.1	2.7	598	$2.6e+06$	16.3	1.12	2862	420	0.45	0.68
3B	170	760	25.4	2.7	600	$4.4e+06$	13.3	0.89	3915	571	0.36	0.59
3C	177	760	–	2.7	601	$8.6e+06$	11.4	0.80	6945	916	0.26	0.65

wall static pressure tap. The freestream temperature was calculated with the definition for the speed of sound, the freestream Mach number and PIV calculated freestream velocity. Finally, assuming an isentropic expansion process, the reservoir pressure and temperature were obtained.

3 PIV setup

3.1 Seeding

Polyalphaolefins (PAO-4) oil particles were used to seed the flow using a TSI Model 9306 atomizer. Tichenor et al. (2011, 2012) reported a mean diameter of $0.25 \mu\text{m}$ for this atomizer. The atomizer output concentration is 4.3×10^6 particles/cc.

Seeding particles were supplied to the tunnel by the global seeder, developed by Brooks et al. (2015). The global seeder shown in Fig. 3 creates a sealed isobaric reservoir for the indraft M3CT. The reservoir consists of a thin-walled pallet-sized ($1.4 \times 1.1 \times 2.5\text{m}^3$) plastic bag positioned vertically with the opening facing down. Particles were first injected into the reservoir. Then, an air pump was used to evenly mix the particles and inflate the bag to the volume necessary for a run. Particle concentration in the reservoir was controlled by the operating time for the particle atomizer during injection. The reservoir concentration was determined based on experience to maintain a high concentration of particles in the image. Rings connected to the pallet bag are constrained to vertically running wire ropes to control the bag deformation as its content empties (similar to a bellows).

Plumbing transports the aerosol to the Mach 3 nozzle through the orifice plate, flow straighteners, and a contoured bell nozzle. The reservoir temperatures in Table 1

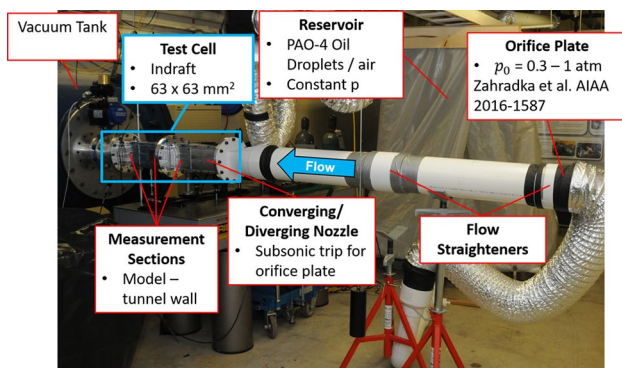


Fig. 3 M3CT test cell showing the installation of the global seeder, flow direction is indicated by arrow. The collapsible reservoir is not visible as it is behind a safety curtain. Key features are indicated in image text boxes

are slightly higher than ambient due to heating from the air pump used to inflate the bag.

Short particle response times are critical for accurate tracking of high-speed flows. Particle response time relative to the flow is quantified through the Stokes number. The Stokes number must be sufficiently small for accurate particle tracking

$$St = \frac{\tau_p}{\tau_f} < 1. \quad (1)$$

In this definition, the flow characteristic time is defined as

$$\tau_f = \frac{\delta}{u_e}. \quad (2)$$

Assuming Stokes flow and a particle density much greater than the flow density, the particle response time can be expressed as Adrian and Westerweel (2011)

$$\tau_p = \left(\frac{d_p^2 \rho_p}{18\mu} \right) (f_{Kn}). \quad (3)$$

The correction term f_{Kn} accounts for rarefaction effects Loth and Introduction (2008) and takes the form

$$f_{Kn} = 1 + Kn_p \left(c_1 + c_2 \left(e^{\frac{c_3}{Kn_p}} \right) \right), \quad (4)$$

where the Knudsen number is

$$Kn_p = \sqrt{\frac{\pi\gamma}{2}} \left(\frac{M_p}{Re_p} \right) \sim \frac{1}{\rho}, \quad (5)$$

and the coefficients are $c_1 = 2.514$ $c_2 = 0.8$ $c_3 = -0.55$. In hypersonic flows, the value of the particle Knudsen number is typically large which significantly increases the particle response time compared to continuum flow, see Williams (2014). For the Tunnel 9 hollow cylinder test condition, the particle response time increases by approximately one order of magnitude.

DNS studies with particle trajectory simulations for a free shear layer by Samimy and Lele (1991) have shown that the velocity error due to the particle relaxation time is proportional to the Stokes number for values of Stokes number up to 1. Note, the Stokes number here is calculated as defined by Eq. 1 which is ten times larger than that published by Samimy and Lele due to the definition of the flow response time.

The experimental cases were designed assuming the reported particle diameter of $0.25 \mu\text{m}$. Using this diameter, the Stokes numbers for all nine cases are all ≤ 0.5 . To verify the diameter, an oblique shock wave test was performed following the methodology of Ragni et al. (2011). The particle response time was calculated from the measured shock

normal relaxation distance behind an oblique shock wave generated by a 8° ramp. Using this particle response time in Eq. 3, the particle diameter is estimated as $d_p \approx 0.5 \mu\text{m}$ which is twice the value reported by Tichenor et al. (2011), Tichenor et al. (2012). This causes the Stokes numbers to increase by roughly a factor of 2–2.5. The Stokes numbers for $d_p = 0.5 \mu\text{m}$ are listed in Table 2.

Using Eq. 3 to find the particle diameter it is assumed that the particle drag is constant and equal to that directly behind the shock. To verify this solution, the quasi-steady analysis of the particle drag was also performed following the methodology of Williams et al. (2015). Williams et al. reported that the constant drag solution under-predicted particle diameter by a factor of ~ 4.5 . For the 8° ramp in the M3CT, the quasi-steady particle diameter agrees very well with the constant drag solution. The Reynolds number of the M3CT is much lower than the Mach 3 case simulated by Williams et al. The initial slip Mach and Reynolds numbers are $M_{s,0} = 0.4$ and $Re_{s,0} = 1.6$. The particle drag for the quasi-steady analysis only increases by 8% throughout the particle response time. Further experiments are necessary to completely characterize the particle response diameter, including multiple ramp angles such as what has been done by Williams et al.

3.2 Optics, laser and post-processing

An integrated design tools (IDT) Os-10 high-speed complementary metal-oxide-semiconductor (CMOS) camera, fitted with a Nikon AF Nikkor 24–85 mm 1:2.8-4 D lens, was used for particle imaging. The camera was selected due to the fast interframe time of 200 ns required for the Tunnel 9 conditions. This camera also has notable benefits over the IDT Y-7 PIV camera previously used for PIV at AEDC by Brooks et al. (2014, 2015, 2016), namely the small $4.67 \times 4.67 \mu\text{m}^2$ pixels, 12 bit pixel depth, and high $3840 \times 2400 \text{ px}^2$ (9.2 Mpx) resolution Integrated Design Tools (2016).

The light sheet was produced with a Litron LPY 703-200 PIV laser, outputting a pair of 50 mJ, 10–12 ns pulses at 200 Hz Litron Lasers North America (2010). The built-in attenuator was used to reduce the laser energy, $\sim 16 \text{ mJ}$. The sheet thickness was 0.9 mm in the test section, as determined using a burn pattern. The laser sheet propagated vertically from the top of the test section through a window insert. Boundary layer measurements were taken off the bottom wall. The Os-10 internal clock controlled the 200 Hz timing between laser pair events. A sync-out pulse from the camera triggered a Stanford Research Systems Inc. Model DG 535 pulse generator, which controlled the laser pulse separation timing. The pulse separation time was verified using a photo diode. A pulse separation time of 400 ns was used for the M3CT to allow for larger wall-normal displacements.

DaVis 8 was used as the image correlation software. First, the location of the wall was determined within one pixel by visual inspection of the laser reflection. The wall position in the image did not vary perceptibly throughout the run. A two-pass method was used to calculate the velocity, starting with $256 \times 256 \text{ px}^2$ windows and ending with $96 \times 96 \text{ px}^2$ windows with 75% overlap. For Exp. 2C, the particles displace 17% of the first-pass windows and 46% of the second pass at this pulse separation time. A 4:1 weight biasing is applied in the streamwise direction. The same interrogation window sizes were used for all camera magnifications to test the effect of the spatial resolution. A four-pass $3 \times 3 \text{ px}^2$ median and minimum peak ratio post-processing filters were used to identify and eliminate erroneous vectors. The PIV frames yielded over 90% valid vectors for $y/\delta > 0.05$.

3.3 Mitigation of laser reflection noise

Two methods were employed to reduce wall reflections to obtain near-wall measurements. Initially, rhodamine paint with a similar formulation as Cadel et al. (2016) was applied to a blank aluminum insert. The rhodamine paint absorbs the 532-nm laser light and fluoresces at a higher wavelength, $>550 \text{ nm}$. Reflection noise was significantly reduced using a $532 \pm 1.5 \text{ nm}$ narrow-band-pass filter in front of the image array. However, the laser ablated the paint over the duration of two or three runs. The second method used a clear polycarbonate insert which increased transmission and, therefore, decreased wall reflections. The sides of the clear insert were painted with rhodamine paint to remove internal reflections from the tunnel wall (seen through the clear insert). The polycarbonate insert method was preferred over rhodamine paint for the M3CT due to the paint ablation.

The maximum extent of noise was reduced to 0.05δ , with a few experiment showing no laser reflection noise. A sliding average subtraction pre-processing filter in DaVis was applied to reduce this noise. Although the noise was significantly reduced, the remaining noise after this filter attributed to an increase in measurement uncertainty near the wall.

4 Measurement uncertainties

The measurement uncertainty analysis investigated both bias and precision uncertainty. Precision uncertainty was determined statistically and incorporates random errors associated with PIV technique such as camera noise, particle out-of-plane motion and inhomogeneous particle density. The precision uncertainty on mean velocities and mean fluctuating velocities was calculated using the equation

$$\overline{P_{u_i}} = 1.96 \sqrt{\text{var}(u_i)}. \quad (6)$$

The velocity variance, $\text{var}(u_i)$, was found using the formulae in Benedict and Gould (1996). Bias uncertainties, systematic errors due to calibration and vector calculation, were estimated at 1%.

The uncertainty was propagated through the data reduction equations as outlined by Coleman and Steele (2009). Uncertainty on the boundary layer, momentum and displacement thicknesses was estimated using the 1/7th power law (Smits and Dussage 2006) since these quantities depend on correlated velocity points in the profile. Flow parameter uncertainties, and velocity and position uncertainties at $y/\delta = 0.5$ for Exp. 2C are presented in Table 3. The starred terms in Table 3 indicate Morkovin (1962)-scaled quantities defined as

$$u'^* = \sqrt{\frac{\rho}{\rho_w} \frac{\sqrt{u'^2}}{u_\tau}}$$

$$v'^* = \sqrt{\frac{\rho}{\rho_w} \frac{\sqrt{v'^2}}{u_\tau}}$$

and

$$(u'v')^* = \frac{\overline{\rho u'v'}}{\tau_w}$$

The uncertainty analysis assumes that the particles accurately follow the flow. The effects of particle lag on the fluctuating velocity are discussed in Sects. 7 and 8.

5 Mean velocity profile

Inner and outer scaling are generally used to analyze turbulent boundary layers. Inner scaling is used near the wall where viscosity is important and has a length scale equal to ν/u_τ . Outer scaling is applicable in the region where turbulent kinetic stresses dominate and has a length scale equal to δ . Both scalings use u_τ as the velocity scale. For incompressible ZPG turbulent boundary layers, Millikan (1938) proposed a

Table 3 Uncertainty values for Exp 2C at $y/\delta = 0.5$

Variable	Uncertainty (%)
$y, y/\delta, y^+$	0.3, 7.2, 10.4
u, u_{vd}^+	1.1, 13.0
u', u'^*	5.7, 12.0
v', v'^*	6.5, 12.4
$u'v', (u'v')^*$	16.5, 22.7
δ	7.2
u_e	1.0
u_τ	10.1

region where both inner and outer scales are simultaneously valid. This region is known as the log layer because dimensional analysis based on inner and outer scaling reveals that the velocity profile has a logarithmic relationship, where

$$u^+ = \frac{u}{u_\tau} = \frac{1}{\kappa} \log \left(\frac{u_\tau y}{\nu_w} \right) + C. \tag{7}$$

The constants in Eq. 7 are nearly universal for incompressible turbulent boundary layers. For this study, we adopt the generally accepted values of $\kappa = 0.40$ and $C = 5.1$. However, there exists some ambiguity regarding their exact values in the literature.

Incompressible theory is extended to compressible flows by modifying the dimensional analysis to account for changes in density using the van Driest effective velocity (1951), defined as

$$u^* = \int_{u_1}^u \sqrt{\frac{\rho}{\rho_w}} du, \tag{8}$$

where u_1 is the streamwise velocity at the lower edge of the log layer. The mean density profile (including ρ_w) is found using temperature determined from the Walz equation (Walz 1969) and the perfect gas law assuming constant pressure throughout the boundary layer. The Walz equation is substituted into Eq. 8 to obtain the closed-form equation

$$u^* = \frac{u_e}{b} \sin^{-1} \left(\frac{2b^2(u/u_e) - a}{\sqrt{a^2 + 4b^2}} \right), \tag{9}$$

where

$$a = \left(1 + r \frac{\gamma - 1}{2} M_e^2 \right) \frac{T_e}{T_w} - 1, \tag{10}$$

$$b^2 = r \frac{\gamma - 1}{2} M_e^2 \left(\frac{T_e}{T_w} \right), \tag{11}$$

and $r = \sqrt[3]{Pr}$ is the recovery factor. For the case of an adiabatic ZPG flat-plate compressible turbulent boundary layer, the recovery temperature is equal to the wall temperature making the term $a = 0$. And, the velocity profile in the log layer is defined as

$$u_{vd}^+ = \frac{u^*}{u_\tau} = \frac{1}{\kappa} \log \left(\frac{u_\tau y}{\nu} \right) + C. \tag{12}$$

where κ and C are the same as defined in Eq. 7.

Coles (1956) extended the log law into the outer scaling region by adding a wake function to describe the departure from the log layer. The derived law of the wake,

$$u_{vd}^+ = \frac{1}{\kappa} \log \left(\frac{u_\tau y}{\nu_w} \right) + C + \frac{2\Pi}{\kappa} \sin^2 \left(\frac{\pi y}{2 \delta_c} \right), \tag{13}$$

is valid from the log layer through to the outer region including the intermediate overlap.

Equations 12 and 13 require the skin friction velocity which is not measured directly. Instead, u_τ is calculated from a nonlinear least squares fit of Eq. 13 to the PIV data. Coles’s law of the wake is preferred because there were more PIV data points over the region where Eq. 13 is valid compared to Eq. 12. Also, the location and extent of the log layer vary with Reynolds number, and diminish at low Reynolds numbers. This would introduce subjectivity in the selection of PIV data used for a fit of Eq. 12.

Following the work of Lewis et al. (1972), the fitting region for the PIV data is limited to $y^+ = u_\tau y / \nu_w > 50$ to avoid points with increased measurement uncertainty near the wall, and $u/ue < 0.98$ as Eq. 13 is not valid at $y = \delta$. The fit to Eq. 13 simultaneously calculates u_τ , the Coles boundary layer thickness δ_c , and the wake strength parameter Π . Agreement between the PIV data and Eq. 13 gives confidence in the measurements. The adjusted coefficient of determination is used to assess the quality of the fit. The adjusted coefficient of determination takes into account the number of data points used for the fit and the number of parameters determined by the fit.

The law of the wake (13) provides an excellent fit to the PIV data. This is evidenced by the adjusted coefficients of determination, $R_{adj}^2 \rightarrow 1.0$, for all flow conditions. Figure 4 shows the very good fit of Coles’s law of the wake to the PIV data with the minimum and maximum Reynolds numbers (Exps. 1A and 3C, respectively). The log layer for Exp. 1A is small, $20 \leq y^+ \leq 50$, and data used for the fit, $y^+ > 50$, are entirely in the wake region. The higher Reynolds number of Exp. 3C extends the log layer to $20 \leq y^+ \leq 200$. As such, the fit uses about ~ 10 data points in the log layer. The fit of Cole’s law of the wake yields equally high coefficients of determination, regardless of the different regions of the boundary layer used for the fit.

Figure 5 shows the PIV velocity with inner scaling for all nine flow conditions. The data sets are grouped by Reynolds number and separated by an offset of 4 and 8 added to the ordinate for the intermediate and high-Reynolds number groups, respectively. The u_{vd}^+ scaling collapses the PIV data very well in the log layer. For comparison, the universal log law is plotted in Figs. 4 and 5.

The skin friction velocity, u_τ , calculated from the fit is within 5% of the van Driest II transformation which is recommended by Hopkins and Inouye (1971) for the determination of supersonic and hypersonic skin friction. The boundary layer thickness determined by the fit δ_c is less than the 99.9% boundary layer thickness δ and is closer to the 99% boundary layer thickness δ_{99} .

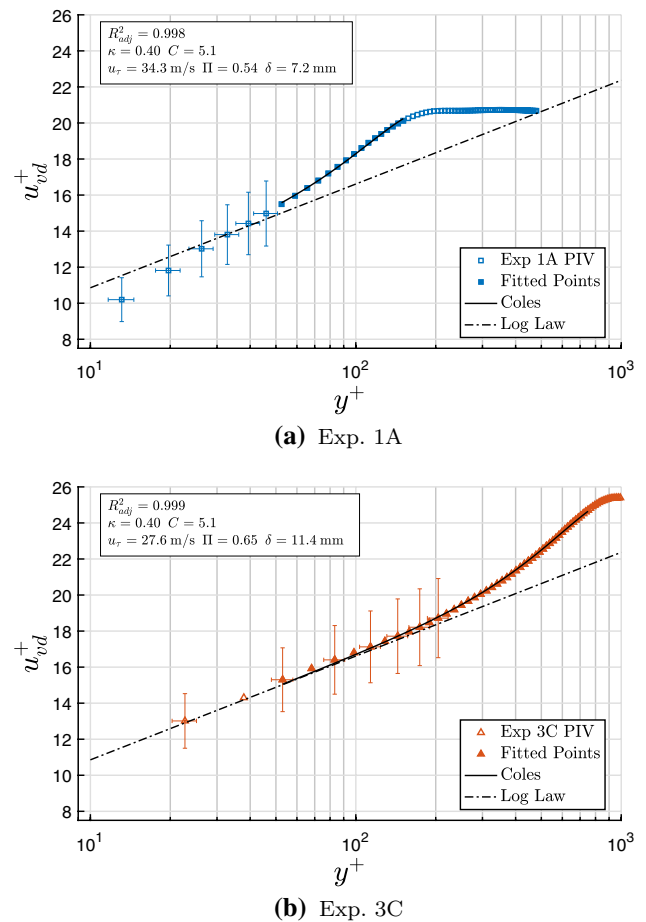


Fig. 4 Inner scaled velocity showing the excellent fit to Coles’s law of the wake, Eq. 13, for PIV Exps. 1A and 3C. The fitted parameters u_τ , δ_c , and Π are shown in the upper left corner. The fitting region included the log layer and wake region for Exp. 3C and only the wake region for Exp. 1A. Error bars are shown for points below the wake region

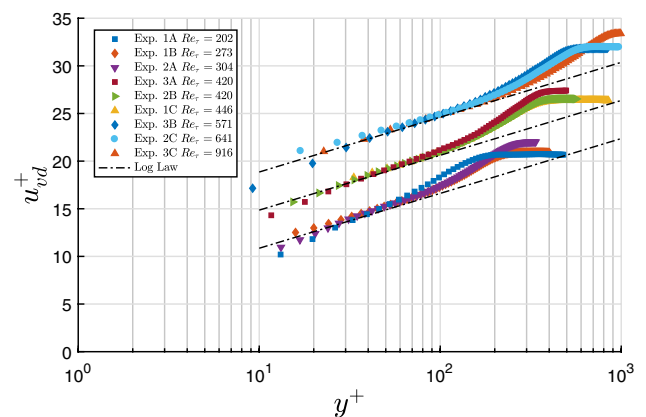


Fig. 5 Streamwise velocity with inner scaling for all flow conditions. Experiments are grouped by Reynolds number and separated by an offset of 4 and 8 added to the ordinate for the intermediate and high-Reynolds number groups. The u_{vd}^+ scaling determined by Coles’s law of the wake fit collapses the data very well in the log layer. The universal log law 12 is shown for comparison

6 Spatial resolution

The spatial resolution, defined as

$$SR = \delta/D_I, \tag{14}$$

relates the boundary layer thickness to the interrogation window size D_I (in object plane). A high spatial resolution implies a large number of velocity vectors in the boundary layer. The spatial resolution also gives an indication of the extent of spatial averaging of the velocity gradient across the interrogation window.

The spatial resolution was investigated in two ways. First, via vector processing where the camera magnification was held constant and the interrogation window size was varied. Second, optically, where the interrogation window size was held constant and the camera magnification was varied.

6.1 Vector processing

The initial analysis was conducted with a rather coarse interrogation window size (128 px 50% overlap), for computational speed. A second, finer data set (96 px 75% overlap) was computed to increase vector resolution and verify there was no loss of information due to velocity averaging in the coarse interrogation windows. In general, the interrogation window size has little effect on the data, as demonstrated in the fluctuating velocity profiles. The post-processing results are similar to Exp 2C, shown in Fig. 6. The magnitudes of the streamwise and wall-normal fluctuating velocity profiles are slightly lower for the coarse grid compared with the fine grid. The effect is small as the differences are less than 7% which is well within the measurement uncertainties. The lower magnitudes are attributed to spatial averaging of finer scale fluctuations over the larger windows.

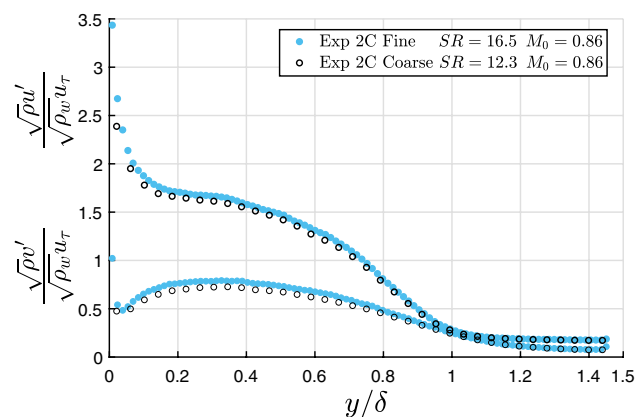


Fig. 6 Streamwise and wall-normal Morkovin-scaled fluctuating velocity profiles comparing the effect of vector processing spatial resolution. There is excellent agreement between the coarse- and fine-grid resolutions. The coarse-grid fluctuating velocity magnitudes are less than the fine but are within 7%

6.2 Magnification

PIV measurements for each of the nine flow conditions were repeated four times with different lens magnifications. All magnifications were processed using 96 px 75% overlapping windows. The data for each flow condition listed in Table 2 are selected based on lowest uncertainty (see Sect. 4) among the camera magnifications, particularly near the wall. The experiment with the highest magnification typically has the lowest uncertainty. Exp. 1A is the exception, where the second highest magnification has the lowest uncertainties.

The streamwise and wall-normal fluctuating velocity magnitudes increase with increasing camera magnification. Figure 7 shows the typical trend exemplified by the four experiments for condition Exp. 1B. The reduced magnitudes are attributed to combined effects of decreased spatial averaging, particle image diameter and particle shift. Contributions of individual effects must be studied further.

7 Velocity fluctuations and Reynolds shear stress

Fluctuating velocity and Reynolds shear stress profiles are compared against experimental data and DNS from the literature listed in Table 4. Two outer length scales δ and δ_{99} are used in the literature to normalize the wall-normal distance. It is important to use the same scaling when comparing profiles to visualize trends in the data because δ is approximately 15% larger than δ_{99} . Data from Ekoto et al. (2007), Elena and LaCharme (1988), Mustafa et al. (2017), Martin (2007), and Klebanoff (1955) used δ as the length scale. Piponniau (2009), Pirozzoli (2011), and Duan et al. (2011) used δ_{99} . Experimental data from Lapsa and Dahm (2011)

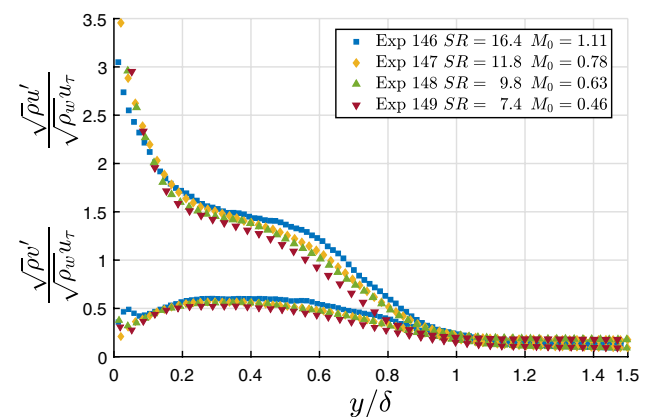


Fig. 7 Streamwise and wall-normal Morkovin-scaled fluctuating velocity profiles showing increasing fluctuating velocity magnitudes with increasing camera magnification. All four experiments have the same conditions as Exp. 1B

Table 4 Key parameters from comparison literature data

		M_e	Re_τ	Re_θ	H	C_f
Ekoto et al. (2007)	PIV	2.86	~4500	60,000	–	–
Elena and LaCharme (1988)	LDV	2.32	~975	4700	3.47	2.15×10^{-3}
Piponniau (2009)	PIV	2.28	1080	5100	3.54	2.00×10^{-3}
Lapsa and Dahm (2011)	PIV	2.75	717	6600	1.4	1.90×10^{-3}
Mustafa et al. (2017)	KTV	2.77	~ 350	1750	–	–
Martin (2007)	DNS	2.32	~ 700	4450	–	–
Pirozzoli (2011)						
<i>a</i>	DNS	2.00	251	1122	3.08	3.19×10^{-3}
<i>b</i>			497	2377	2.98	2.67×10^{-3}
<i>c</i>			1116	6046	2.91	2.11×10^{-3}
Duan et al. (2011)	DNS	2.97	487	3028	5.09	2.17×10^{-3}

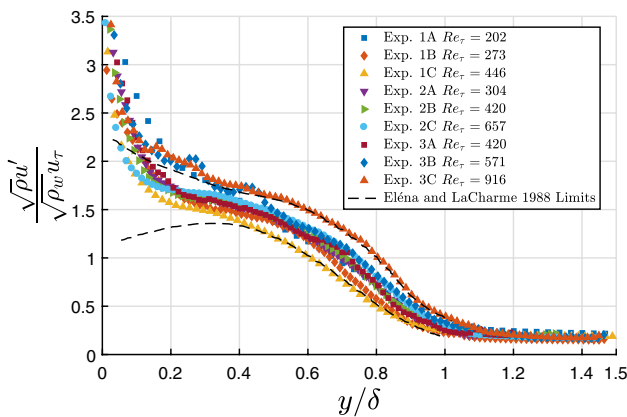


Fig. 8 Morkovin-scaled streamwise fluctuating velocity profiles showing low standard deviation between the nine experimental cases

at the $x/\delta_0 = 40.0$ measurement location used a boundary layer calculated from a fit of the Coles law of the wake. As mentioned in Sect. 5, δ_c was similar to δ_{99} . Therefore, these data are included on the δ_{99} plot. The data presented in this paper are primarily scaled by δ . The data are rescaled by δ_{99} on a separate plot for comparison. Comparison to the krypton tagging velocimetry (KTV) data from Mustafa et al. (2017) is particularly interesting as these data were acquired in the same wind tunnel at similar conditions.

7.1 Streamwise fluctuating velocity

Figure 8 presents the Morkovin-scaled streamwise fluctuating velocity profiles as a function of y/δ for the nine cases listed in Table 2. The streamwise fluctuating velocity profiles for $y/\delta > 0.2$ are all within the limits established by Elena and LaCharme (1988) and the standard deviation for the nine experimental cases are within approximately 10%. Exps. 1C and 3C display the same trend but have the largest deviation from the mean. The outer scaling (y/δ) is not expected to collapse the data in the near-wall region

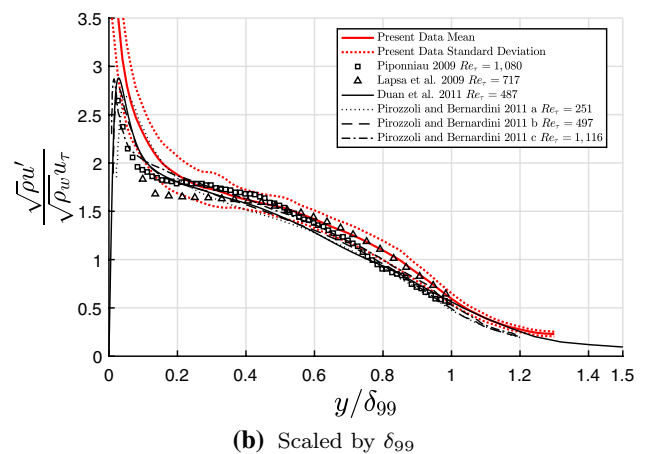
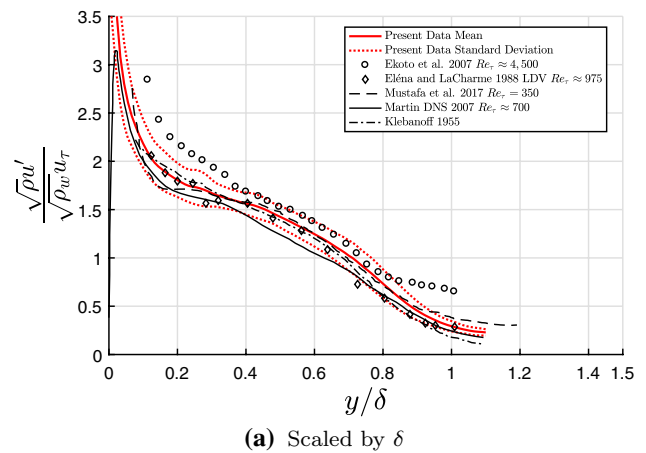


Fig. 9 Streamwise Morkovin-scaled fluctuating velocity profiles compared to experimental and DNS literature data

($y/\delta < 0.1$) as demonstrated by the DNS data in Fig. 9. In addition, the increased deviations near the wall (between 15 and 25%) could be attributed to higher measurement uncertainty due to large velocity gradients, laser reflection, and lag from increased particle response time.

Figure 9a compares the mean of the nine experimental cases to experimental data from the literature and DNS from Martin (2007). Good agreement is seen among the different data sets. Notably, the data from Mustafa et al. (2017) have excellent agreement with the current PIV experiments.

There is also very good agreement between the PIV data and literature scaled by δ_{99} , as shown in Fig. 9b. This plot includes DNS data over a wide range of Re_τ from Pirozzoli (2011) and Duan et al. (2011). As previously mentioned, the outer scaling successfully collapses the DNS away from the near-wall region ($y/\delta > 0.15$).

Figure 10 compares the inner scaled DNS data from Pirozzoli (2011) to the PIV cases at similar Re_τ . Outside of the viscous sublayer ($y^+ > \sim 10$), the inner scaled wall-normal distance y^+ illustrates the effect of Reynolds number on the streamwise fluctuating velocity. The PIV data are distributed in between the DNS as expected based on the Reynolds number, particularly Exp. 2B. Exp. 1B agrees well with Pirozzoli and Bernardini (a) up to $y^+ \approx 100$. Similarly, Exp. 3C has good agreement to Pirozzoli et al. (c) for $y^+ < 300$. The increased deviations between the PIV data and DNS from the literature near the wall ($y^+ < 100$) could be attributed to higher measurement uncertainties, laser reflection, and particle lag.

7.2 Wall-normal fluctuating velocity

Figure 11 presents the Morkovin-scaled wall-normal fluctuating velocity profiles as a function of y/δ for the nine cases listed in Table 2. In addition, HWA data from Klebanoff (1955) are presented for comparison. The standard deviation is larger (approximately 20%) for the wall-normal component compared to the streamwise component. All cases show lower peak magnitudes than Klebanoff with the mean approximately 30% lower throughout the boundary layer. Exp 3C shows the

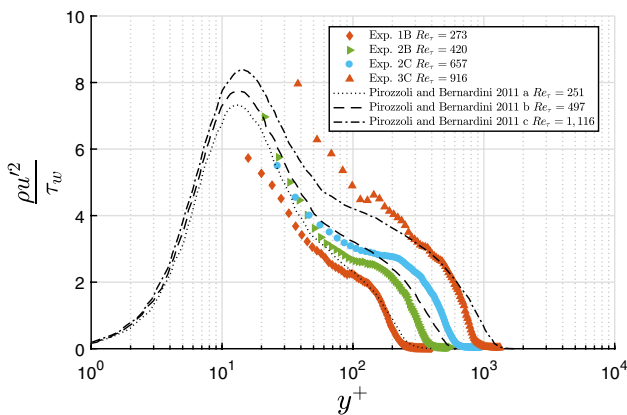


Fig. 10 Streamwise fluctuating velocity profiles with inner scaling emphasizing effect of Reynolds number. Overall, the PIV data are distributed as expected compared to DNS data from Pirozzoli (2011)

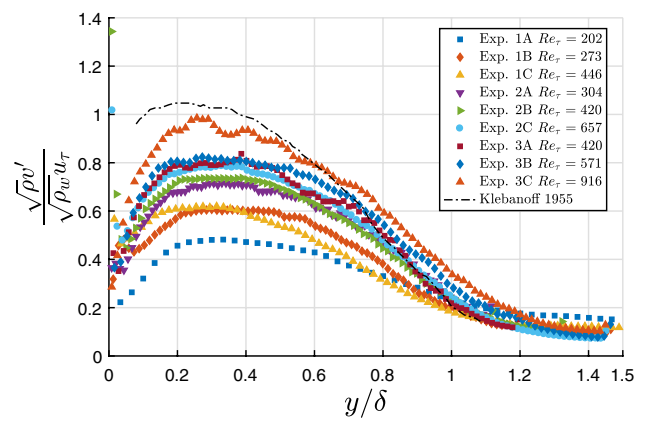


Fig. 11 Morkovin-scaled wall-normal fluctuating velocity profiles showing increased standard deviation between the nine experimental cases compared to the streamwise component

best agreement with Klebanoff. This experiment has the lowest Stokes number ($St = 0.26$). In contrast, Exp 1A with the largest Stokes number ($St = 1.09$) has the worst agreement with Klebanoff.

The effect of the Stokes number on the accuracy of the wall-normal component is investigated in Fig. 12 which presents the relative error between the nine PIV cases and HWA data from Klebanoff (1955) at $y/\delta = 0.2$. The relative error to Klebanoff, $\epsilon(x)$, is defined as

$$\epsilon(x) = \frac{(x)_{Klebanoff} - (x)_{PIV}}{(x)_{Klebanoff}}, \tag{15}$$

where in this case $(x) = v'$. The plot shows a linear increase of the relative error with Stokes number. A linear relationship exists through $y/\delta < 0.9$. The slope of which is constant

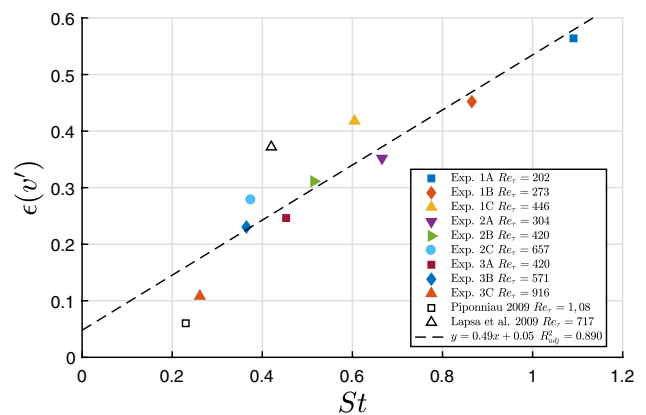
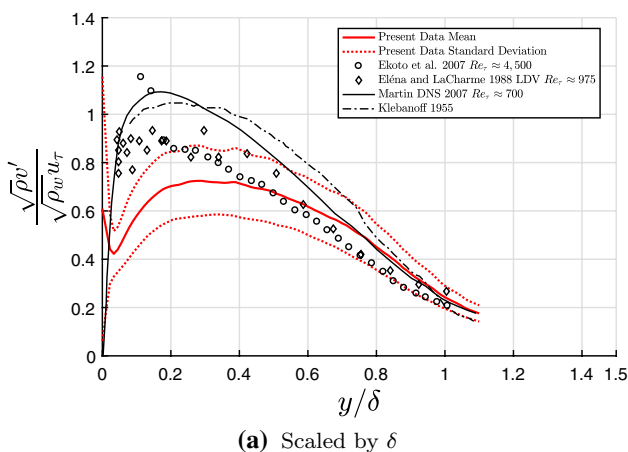


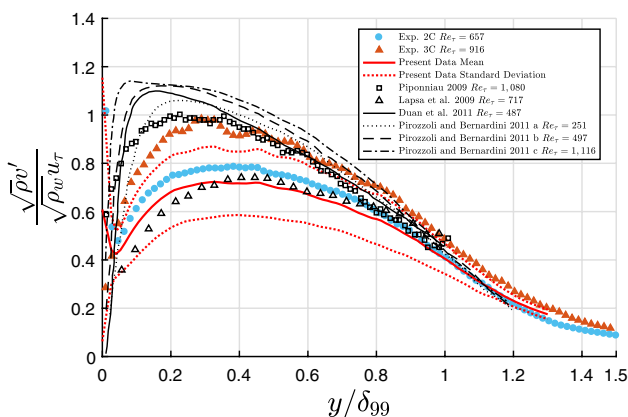
Fig. 12 Relative error in wall-normal Morkovin-scaled fluctuating velocity between the nine PIV cases and Klebanoff HWA data Klebanoff (1955) at $y/\delta = 0.2$. There is a linear trend with the Stokes number. Particle lag was shown to reduce the v' magnitude by Lowe et al. (2014), Williams (2014), and Brooks et al. (2015)

at ≈ 0.5 for $y/\delta < 0.75$. Such a trend is not found for the streamwise component. Attenuated values of the wall-normal fluctuating velocity have been attributed to particle lag by Lowe et al. (2014), Williams (2014), and Brooks et al. (2015). However, prior to the current study, no detailed study characterizing the effect of the Stokes number on the attenuation of the wall-normal fluctuating velocities has been performed experimentally. Data points from Piponniau and Lapsa et al. are also included in Fig. 12. To compare to Klebanoff, the y/δ_{99} profiles were scaled by 85% which is the average decrease from δ to δ_{99} in the current data. These points display a similar trend as the current data, although are not included for the determination of the linear trend line.

Figure 13 compares the mean of the nine experimental cases to experimental data and DNS from the literature. In Fig. 13a, the mean values are approximately 30% lower than the HWA data from Klebanoff (1955) and the DNS from the literature. As for the streamwise component, the DNS from Pirozzoli (2011) show that the outer scaling successfully collapses the wall-normal component away from the near-wall



(a) Scaled by δ



(b) Scaled by δ_{99}

Fig. 13 Wall-normal Morkvin-scaled fluctuating velocity profiles compared to experimental and DNS literature data

region ($y/\delta > 0.15$). This collapse strengthens the notion that the large standard deviation in the wall-normal fluctuations among the nine experimental cases is indeed due to the large range of Stokes numbers. The effect of the Stokes number is also displayed in PIV data from Piponniau (2009) and Lapsa and Dahm (2011). Piponniau reports a Stokes number of $St = 0.23$ whereas Lapsa et al. have a Stokes number of $St = 0.42$. The higher Stokes number from Lapsa et al. has the same effect on the fluctuating velocity magnitudes as the current data. Furthermore, the closest matching Stokes number cases, Exp. 3C with $St = 0.26$ and Exp. 2C with $St = 0.37$, are included in Fig. 13b. There is excellent agreement between PIV data with similar Stokes numbers.

7.3 Reynolds shear stress

Figure 14 presents the Morkvin-scaled Reynolds shear stress profiles as a function of y/δ for the nine cases listed in Table 2. Again, the HWA data from Klebanoff (1955) are presented for comparison. The standard deviation of the nine cases is approximately 25% which is slightly higher than the wall-normal fluctuating velocity. However, the mean values agree better with the Klebanoff data. The mean stress at $y/\delta = 0.2$ is approximately 20% lower than Klebanoff.

Figure 15 shows the relative error between eight of the PIV cases and HWA data from Klebanoff at $y/\delta = 0.2$. Experiment 3C is excluded from this plot. The amount of amplification in Exp 3C may indicate increased noise and not accurately represent the effect of the particle response. The Reynolds stress profiles do not exhibit as strong of a dependence on Stokes number as the wall-normal fluctuating velocity. There is still a visible trend but the coefficient of determination is lower for the Reynolds stress than for the wall-normal component. In addition, the linear relationship exists only for $y/\delta < 0.4$ with a constant slope of ≈ 0.4 . The relationship could be complicated by the fact that the Reynolds stress is the product of

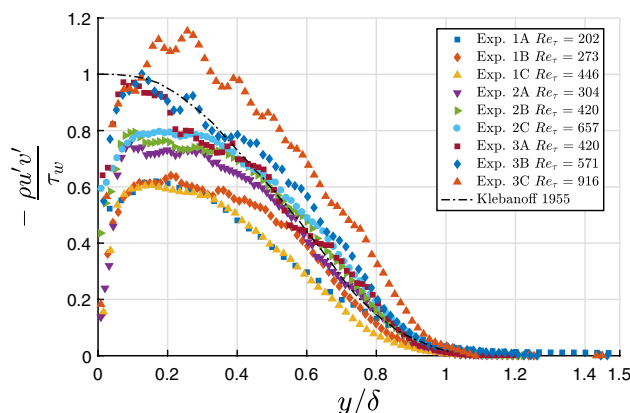


Fig. 14 Morkvin-scaled Reynolds shear stress comparing flow conditions and Klebanoff (1955) data

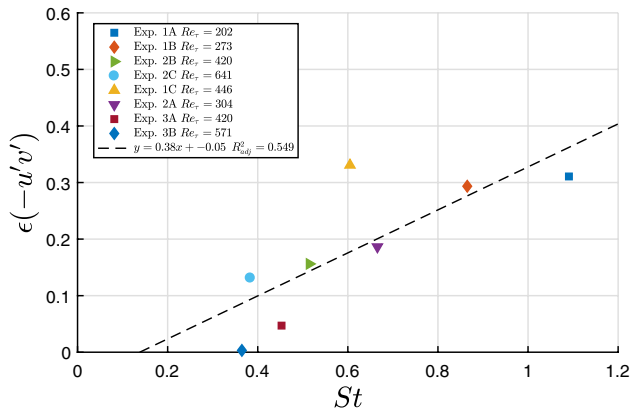


Fig. 15 Relative error in Morkvin-scaled Reynolds shear stress between the nine PIV cases and Klebanoff HWA data Klebanoff (1955) at $y/\delta = 0.2$

u' which is insensitive to the Stokes number and v' which is sensitive. The reason for the abnormally high error in Exp. 1C is unknown.

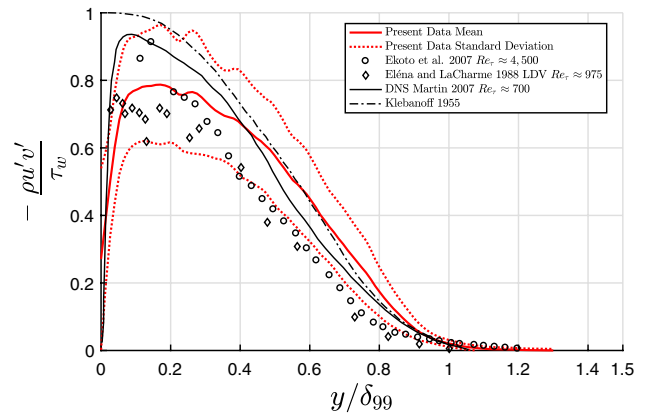
Figure 16 compares the mean of the nine experimental cases to experimental data and DNS from the literature. The agreement with experimental data from the literature shown in Figure 16a is assumed coincidental as these profiles are consistently lower than the DNS throughout the boundary layer. In Fig. 16b, the mean Reynolds stress shows good agreement with DNS data from the literature and experimental data from Piponniau (2009) for $y/\delta > 0.5$. As the wall is approached, the mean measured stress begins to undershoot these data.

8 Spectral density and analysis of large-scale motion structures

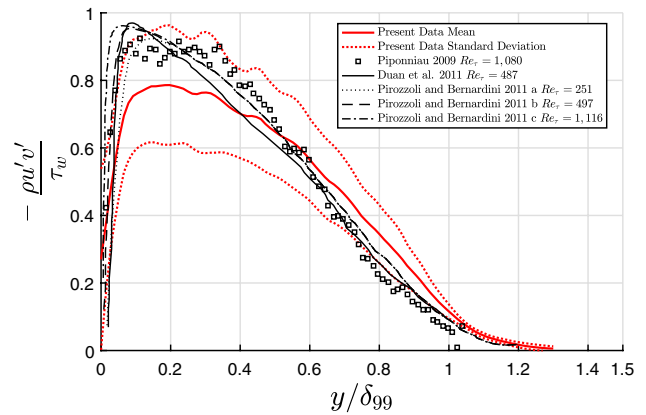
The power spectral density (PSD) of the velocity fluctuations shows the distribution of turbulent kinetic energy in relation to turbulence scale size. The PSD was calculated using a periodogram with hamming windows. The signal for the periodogram was the PIV fluctuating velocity spatially correlated along the streamwise direction at a single y/δ row. This transforms the spatial distribution of velocity fluctuations directly to frequency in wave number space without assuming a convection velocity. A PSD was calculated for each image pair and averaged. The wave numbers for which the PSD is accurately resolved using PIV is limited by two factors, particle response and interrogation window resolution.

The limit based on the interrogation window resolution was determined based on a similar concept as the Nyquist frequency, where

$$k_{\text{cutoff},w} = \frac{2\pi}{2D_I} \tag{16}$$



(a) Scaled by δ



(b) Scaled by δ_{99}

Fig. 16 Reynolds shear stress profiles compared with literature data

For lower spatial resolutions, this becomes the limiting wave number.

The particle response limit was determined using the method outlined by Mei (1996). The particle response function is assumed to be defined by

$$H_p(\omega) = \frac{1 + \epsilon - i\epsilon - i\frac{2}{3}\epsilon^2}{1 + \epsilon - i\epsilon - i\frac{4}{9}(\bar{\rho} + \frac{1}{2})\epsilon^2} \tag{17}$$

where

$$\epsilon = \left(\frac{\omega d_p^2}{8\nu_f} \right)^{1/2} = \left(\frac{9}{4} \frac{\omega \tau_p}{\bar{\rho}} \right)^{1/2} \tag{18}$$

and

$$\bar{\rho} = \frac{\rho_p}{\rho_f} \tag{19}$$

The Knudsen number-corrected particle response time, τ_p , was used in Eq. 17 instead of the shorter Stokes flow particle

response. The useful range of the particle response function for PIV is between

$$\frac{1}{2} < |H_p|^2 < 1. \tag{20}$$

The cutoff frequency, ω , was calculated by solving Eq. 17 for $|H_p|^2 = 0.5$. The cutoff wave number was determined from Taylor’s frozen turbulence hypothesis Taylor (1937), assuming a convection velocity of 85% of the freestream

$$k_{\text{cutoff,p}} = \frac{\omega}{0.85u_e}. \tag{21}$$

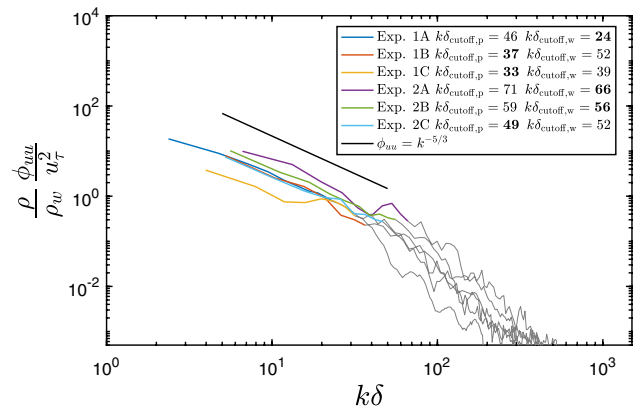
The large ratio of densities, $\bar{\rho} \approx \mathcal{O}(10^4)$, was the driving factor for the particle response wave number cutoff. The limiting wave number is taken as the minimum of the interrogation resolution and particle response cutoff wave numbers.

Figure 17 shows the streamwise and wall-normal PSD with Morkovin scaling at $y/\delta = 0.3$ for Sta. 1 and 2. Experiments at Sta. 3 have been omitted from this comparison due to the reduced usable FOV required to exclude disturbances from the wind tunnel diffuser. Wave numbers within the measurable limit are shown in color, while those above the limit are grayed out. The increased steepness of the slope in the grayed out sections of Fig. 17 is indicative of the particle lag and spatial averaging. The streamwise power spectra density in the measurable data region adheres to a $k^{-5/3}$ decay. The wall-normal decay is closer to k^{-1} , indicating there is more energy at higher wave numbers that has not been measured. This could explain why the wall-normal component has a greater sensitivity to particle lag as discussed by Lowe et al. (2014).

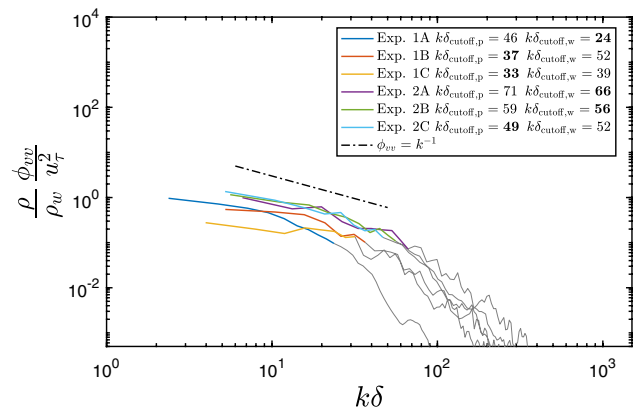
Large-scale motion (LSM) of coherent turbulent structures were identified through PIV using two-point spatial correlations of streamwise velocity fluctuations for the entire field of view (FOV). The spatial correlation coefficient was calculated as

$$R_{uu} = \frac{u'(x, y)u'(x + \Delta x, y + \Delta y)}{\sqrt{[u'(x, y)]^2} \sqrt{[u'(x + \Delta x, y + \Delta y)]^2}}. \tag{22}$$

The reference streamwise location was taken as the middle of the FOV and wall-normal location chosen as desired. Figure 18a shows a contour plot of the spatial correlation coefficient for Exp. 2A at $y/\delta = 0.2$ compared to KTV data from Mustafa et al. (2017) and DNS data from Duan et al. (2011). Figure 18b shows the streamwise decay of the correlation coefficient at $y/\delta = 0.2$. The structure angle describes the upstream lean of the coherent hairpin turbulence packets as described by Perry and Chong (1982) at the given y/δ location. The angle was calculated from the rotation of ellipses



(a) Streamwise fluctuating velocity



(b) Wall-normal fluctuating velocity

Fig. 17 Power spectral density of the velocity fluctuations at $y/\delta = 0.3$ showing the energy content at a given wave number. The wave number is limited by the minimum cutoff value between the particle response and the interrogation window resolution, with values below the limit shown in color, and above grayed out. Measured energy content is larger for higher cutoff wave number experiments. Experiments at Sta. 3 omitted

that were fitted to the isocontours of the correlation coefficient. The rotation angles were averaged for ellipses that fit well to the data. Contour levels above $R_{uu} = 0.7$ were generally avoided because the reduced number of points near the correlation peak center increases uncertainty in the angle.

Figure 18 shows good agreement between the current PIV measurements and the KTV measurements from Mustafa et al. (2017). Exp. 2A is used for this comparison because it used the same orifice plate and measurement location as the KTV data. The PIV data also agree well with DNS data from Duan et al. (2011). The extent of the correlation was similar in streamwise and wall-normal directions. In addition, the calculated angle of 9.6° agrees well with $\sim 9.5^\circ$ angles presented by Peltier et al. (2012) at Mach 5 for the smooth wall case.

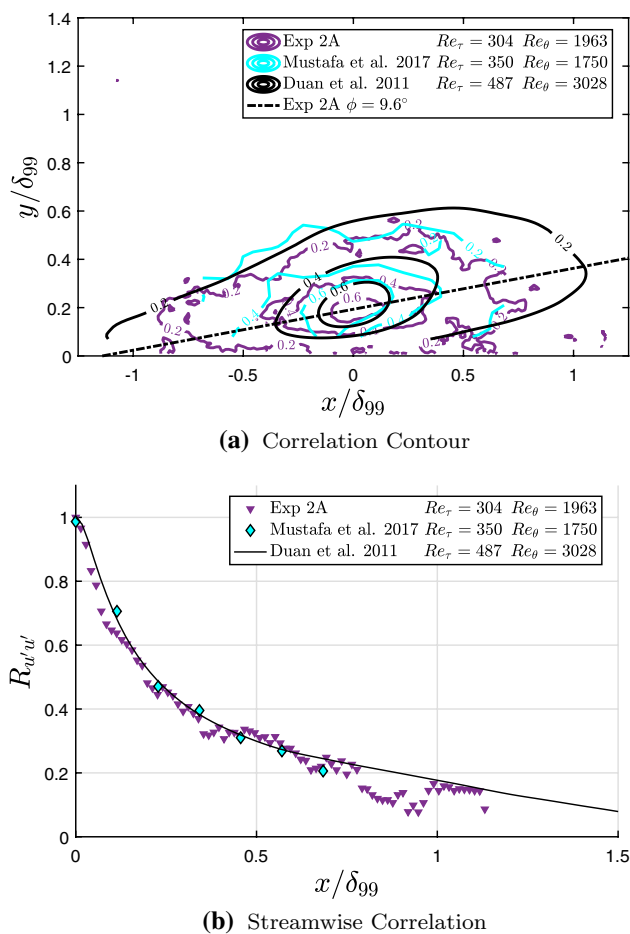


Fig. 18 Two-point spatial correlation R_{uu} vs. downstream streamwise distance at $y/\delta = 0.2$ showing excellent agreement of the PIV data to KTV data Mustafa et al. (2017) measured on the same wind tunnel and DNS data from Duan et al. The dash-dotted line shows the structure angle of 9.6° Duan et al. (2011)

9 Conclusions

PIV measurements were performed in a Mach 3 turbulent boundary layer at Reynolds numbers within a range characteristics of DNS calculations and lower than many experiments reported in the literature. Multiple reservoir pressures and measurement locations create an overlapping parameter space so that flow parameters are isolated from experimental setup and method. The van Driest transformed inner scaled velocity shows excellent agreement to a ZPG adiabatic turbulent boundary layer data. The post-processing spatial resolution (pixels per interrogation window) has a small effect on the fluctuating velocity profiles. However, fluctuating velocity magnitudes increase with camera magnification.

Streamwise fluctuating velocity profiles agree with the literature including low Reynolds number DNS. The wall-normal fluctuating velocity shows a larger variation between experiments compared to the streamwise component. This

variation seems to be due to the particle lag as a linear variation is found between the measurement error and the Stokes number. This agrees with previous studies that show the wall-normal fluctuating velocity is susceptible to particle lag, Lowe et al. (2014), Williams (2014), and Brooks et al. (2015). The error between the wall-normal component and Klebanoff HWA data Klebanoff (1955) is about 10% for $St \approx 0.25$ whereas it exceeds 50% for $St \approx 1$. Energy content at higher wave numbers is found to exceed the measurable range of PIV due to the effects of particle lag and spatial resolution acting as low-pass filters. The flatter spectrum of the wall-normal fluctuating velocity seems to cause this component to be more susceptible to these effects than the streamwise component. The structure angle of coherent turbulent hairpin structures and the extent of the streamwise spatial correlation agree well with that reported in the literature (Duan et al. 2011; Peltier et al. 2012) including the KTV data from Mustafa et al. (2017) performed at the same facility.

References

- Adrian RJ, Westerweel J (2011) Particle image velocimetry. Cambridge University Press, New York
- America Litron Lasers North (2010) Lasers for PIV applications. Bozeman, Montana
- Benedict LH, Gould RD (1996) Towards better uncertainty estimates for turbulence statistics. *Exp Fluids* 22:129–136
- Brooks J, Gupta AK, Helm C, Martin MP, Smith M, Marineau E (2017) Mach 10 PIV Flow Field Measurements of a Turbulent Boundary Layer and Shock Turbulent Boundary Layer Interaction. In: 33rd AIAA Aerodynamic Measurement Technology and Ground Testing Conference. AIAA 2017-3325, Denver, Colorado, USA. <https://doi.org/10.2514/6.2017-3325>
- Brooks JM, Gupta AK, Smith MS, Marineau EC (2014) Development of Non-Intrusive Velocity Measurement Capabilities at AEDC Tunnel 9. In: 52nd AIAA Aerospace Sciences Meeting. AIAA 2014-1239, National Harbor, Maryland, USA. <https://doi.org/10.2514/6.2014-1239>
- Brooks JM, Gupta AK, Smith MS, Marineau EC (2015) Development of particle image velocimetry in a Mach 2.7 wind tunnel at AEDC white oak. In: 53rd Aerospace Sciences Meeting. AIAA 2015-1915, Kissimmee, Florida, USA. <https://doi.org/10.2514/6.2015-1915>
- Brooks JM, Gupta AK, Smith MS, Marineau EC (2016) PIV measurements of mach 2.7 turbulent boundary layer with varying Reynolds numbers. In: 54th AIAA Aerospace Sciences Meeting. AIAA 2016-1147, San Diego, California, USA. <https://doi.org/10.2514/6.2016-1147>
- Cadel DR, Shin D, Lowe KT (2016) A hybrid technique for laser flare reduction. In: 54th AIAA Aerospace Sciences Meeting. AIAA 2016-0788, San Diego, California, USA. <https://doi.org/10.2514/6.2016-0788>
- Coleman HW, Steele WG (2009) Experimentation, validation, and uncertainty analysis for engineers. Wiley, Hoboken
- Coles D (1956) The law of the wake in the turbulent boundary layer. *J Fluid Mech* 1:191–226

- Devenport W, Schetz J (1998) Boundary layer codes for students in Java. In: 1998 ASME Fluids Engineering Division Summer Meeting. FEDSM98-5139, Washington, DC, USA
- Devenport WJ, Schetz JA, Wang Y (1999) Heat transfer codes for students in Java. In: 5th ASME/JSME Thermal Engineering Joint Conference. AJTE99-6229, San Diego, California, USA
- Duan L, Beekman I, Martin M (2011) Direct numerical simulation of hypersonic turbulent boundary layers. Part 3. Effect of Mach number. *J Fluid Mech* 672:245–267. <https://doi.org/10.1017/S0022112010005902>
- Ekoto IW, Bowersox RDW, Goss L (2007) Mach 10 PIV flow field measurements of a turbulent boundary layer and shock turbulent boundary layer interaction. In: 45th AIAA Aerospace Sciences Meeting and Exhibit. AIAA 2007-1137, Reno, Nevada, USA. <https://doi.org/10.2514/6.2007-1137>
- Elena M, LaCharme JP (1988) Experimental study of a supersonic turbulent boundary layer using a laser Doppler anemometer. *J Theor Appl Mech* 7(2):175–190
- Fernholz HH, Finley PJ (1980) A critical commentary on mean flow data for two-dimensional compressible turbulent boundary layers. Tech. Rep. AGARDograph No. 253, Advisory Group for Aerospace Research and Development, Neuilly sur Seine (1980)
- Hopkins EJ, Inouye M (1971) An Evaluation of Theories for Predicting Turbulent Skin Friction and Heat Transfer on Flat Plates at Supersonic and Hypersonic Mach Numbers. *AIAA J* 9(6):993–1003
- Integrated Design Tools (2016) OS10-V3-4K Specification Sheet. Tallahassee, Florida, USA. https://tdtvision.com/support/specifications-sheets/?idt_id=OS10-V3-4K
- Kistler AL (1959) Fluctuation measurements in a supersonic turbulent boundary layer. *Phys Fluids* 2(3):290–296. <https://doi.org/10.1063/1.1705925>
- Klebanoff PS (1955) Characteristics of turbulence in a boundary layer with zero pressure gradient. Tech. Rep. NACA-TR-1247, National Advisory Committee for Aeronautics, Springfield, Virginia, USA
- Lapsa AP, Dahm WJA (2011) Stereo particle image velocimetry of nonequilibrium turbulence relaxation in a supersonic boundary layer. *Exp Fluids* 50(1):89–108. <https://doi.org/10.1007/s00348-010-0897-x>
- Lewis JE, Gran RL, Kubota T (1972) An experiment on the adiabatic compressible turbulent boundary layer in adverse and favourable pressure gradients. *J Fluid Mech* 51(4):657–672
- Loth E, Introduction I (2008) Compressibility and rarefaction effects on drag of a spherical particle. *AIAA J* 46(9):2219–2228. <https://doi.org/10.2514/1.28943>
- Lowe KT, Byun G, Simpson RL (2014) supersonic turbulent boundary layer statistics. In: 52nd AIAA Aerospace Sciences Meeting. AIAA 2014-0233, National Harbor, Maryland, USA
- Martin MP (2007) Direct numerical simulation of hypersonic turbulent boundary layers. Part 1. Initialization and comparison with experiments. *J Fluid Mech* 570:347–364. <https://doi.org/10.1017/jfm.2011.252>
- Mei R (1996) Velocity fidelity of flow tracer particles. *Exp Fluids* 22:1–13
- Millikan CBA (1938) A critical discussion of turbulent flows in channels and circular tubes. In: Proceedings of the Fifth International Congress of Applied Mechanics, pp 386–392
- Morkovin MV (1962) Effects of compressibility on turbulent flows. In: Favre AJ (ed) *Mecanique de la Turbulence*. Centre National de la Recherche Scientifique (CNRS), pp 367–380
- Mustafa MA, Hunt MB, Parziale NJ, Smith MS, Marineau EC (2017) Krypton Tagging Velocimetry (KTV) Investigation of Shock-Wave/Turbulent Boundary-Layer Interaction. In: 55th AIAA Aerospace Sciences Meeting, January. AIAA 2017-0025, Grapevine, Texas, USA. <https://doi.org/10.2514/6.2017-0025>
- Peltier S, Humble RA, Bowersox RDW (2012) PIV of a Mach 5 Turbulent Boundary Layer over Diamond Roughness Elements. In: 42nd AIAA Fluid Dynamics Conference and Exhibit. AIAA 2012-3061, New Orleans, Louisiana, USA. <https://doi.org/10.2514/6.2012-3061>
- Perry AE, Chong MS (1982) On the mechanism of wall turbulence. *J Fluid Mech* 119:173–217. <https://doi.org/10.1017/s0022112082001311>
- Piponniau S (2009) Instationnarité dans les décollements compressibles: cas des couches limites soumises à une onde de choc. Université de Provence-Aix-Marseille, Docteur
- Pirozzoli S, Bernardini M (2011) Turbulence in supersonic boundary layers at moderate Reynolds number. *J Fluid Mech* 688(2011):120–168. <https://doi.org/10.1017/jfm.2011.368>
- Pirozzoli S, Bernardini M (2013) Probing high-Reynolds-number effects in numerical boundary layers. *Phys Fluids* 021704(25):1–7. <https://doi.org/10.1063/1.4792164>
- Ragni D, Schrijer F, Oudheusden BWV, Scarano F (2011) Particle tracer response across shocks measured by PIV. *Exp Fluids*. <https://doi.org/10.1007/s00348-010-0892-2>
- Samimy K, Lele SK (1991) Motion of particles with inertia in a compressible. *Phys Fluids A* 3(8):1915–1923. <https://doi.org/10.1063/1.857921>
- Smits AJ, Dussage JP (2006) *Turbulent Shear Layers in Supersonic Flow*, 2nd edn. Springer, New York
- Smits AJ, Hayakawa K, Muck KC (1983) Constant temperature hot-wire anemometer practice in supersonic flows- Part I: the normal wire. *Exp Fluids* 1(2):83–92. <https://doi.org/10.1007/BF00266260>
- Taylor GI (1937) The spectrum of turbulence. *Proc R Soc Lond A* 164(919):476–490
- Tichenor NR, Humble RA, Bowersox RDW (2011) Influence of Favorable Pressure Gradients on a Mach 5.0 Turbulent Boundary Layer. In: 49th AIAA Aerospace Sciences Meeting including the New Horizons Forum and Aerospace Exposition. AIAA 2011-0748, Orlando, Florida, USA
- Tichenor NR, Humble RA, Bowersox RDW (2012) Reynolds Stresses in a Hypersonic Boundary Layer with Streamline Curvature—Driven Favorable Pressure Gradients. In: 42nd AIAA Fluid Dynamics Conference and Exhibit. AIAA 2012-3059, New Orleans, Louisiana, USA
- Townsend AA (1951) The structure of the turbulent boundary layer. *Math Proc Cambridge Philos Soc* 47:375–395. <https://doi.org/10.1017/s0305004100026724>
- van Driest ER (1951) Turbulent boundary layer in compressible fluids. *J Aeronaut Sci* 18(3):145–160
- Walz A (1969) *Boundary layers of flow and temperature*. MIT Press, Cambridge
- Williams OJH (2014) Density effects on turbulent boundary layer structure: from the atmosphere to hypersonic flow. Doctoral dissertation, Princeton University
- Williams OJH, Nguyen T, Schreyer AM, Smits AJ (2015) Particle response analysis for particle image velocimetry in supersonic flows. *Phys Fluids* 27:076101. <https://doi.org/10.1063/1.4922865>
- Williams OJH, Sahoo D, Baumgartner M, Smits AJ (2018) Experiments on the structure and scaling of hypersonic turbulent boundary layers. *J Fluid Mech* 834:237–270
- Zahradka D, Parziale NJ, Smith MS, Marineau EC (2016) Krypton tagging velocimetry in a turbulent Mach 2.7 boundary layer. *Exp Fluids* 57(5):1–14. <https://doi.org/10.1007/s00348-016-2148-2>